

MOIRCS Deep Survey. VII: NIR Morphologies of Star-forming Galaxies at Redshift $z \sim 1$

Masahiro KONISHI,^{1,2} Masayuki AKIYAMA,³ Masaru KAJISAWA,³ Takashi ICHIKAWA,³
Ryuji SUZUKI,² Chihiro TOKOKU,³ Yuka KATSUNO UCHIMOTO,¹ Tomohiro YOSHIKAWA,³
Ichi TANAKA,² Masato ONODERA,⁴ Masami OUCHI,⁵ Koji OMATA,² Tetsuo NISHIMURA,²
and Toru YAMADA³

¹*Institute of Astronomy, University of Tokyo, Mitaka, Tokyo 181-0015, Japan*
konishi@ioa.s.u-tokyo.ac.jp

²*Subaru Telescope, National Astronomical Observatory of Japan, 650 North A'ohoku Place, Hilo, HI 96720, USA*

³*Astronomical Institute, Tohoku University, Aramaki, Aoba, Sendai 980-8578, Japan*

⁴*CEA-Saclay, DSM/DAPNIA/Service d'Astrophysique, 91191 Gif-sur-Yvette Cedex, France*

⁵*Observatories of the Carnegie Institution of Washington, 813 Santa Barbara Street, Pasadena, CA 91101, USA*

(Received ; accepted)

Abstract

We investigate rest-frame near-infrared (NIR) morphologies of a sample of 139 galaxies with $M_s \geq 1 \times 10^{10} M_\odot$ at $z=0.8-1.2$ in the GOODS-North field using our deep NIR imaging data (MOIRCS Deep Survey, MODS). We focus on Luminous Infrared Galaxies (LIRGs), which dominate high star formation rate (SFR) density at $z \sim 1$, in the sample identified by cross-correlating with the *Spitzer*/MIPS $24\mu\text{m}$ source catalog. We perform two-dimensional light profile fitting of the $z \sim 1$ galaxies in the K_s -band (rest-frame J -band) with a single component Sérsic model. We find that at $z \sim 1$, $\sim 90\%$ of LIRGs have low Sérsic indices ($n < 2.5$, similar to disk-like galaxies) in the K_s -band, and those disk-like LIRGs consist of $\sim 60\%$ of the whole disk-like sample above $M_s \geq 3 \times 10^{10} M_\odot$. The $z \sim 1$ disk-like LIRGs are comparable or $\sim 20\%$ small at a maximum in size compared to local disk-like galaxies in the same stellar mass range. If we examine rest-frame UV–optical morphologies using the *HST*/ACS images, the rest-frame B -band sizes of the $z \sim 1$ disk-like galaxies are comparable to those of the local disk-like galaxies as reported by previous studies on size evolution of disk-like galaxies in the rest-frame optical band. Measuring color gradients (galaxy sizes as a function of wavelength) of the $z \sim 1$ and local disk-like galaxies, we find that the $z \sim 1$ disk-like galaxies have 3–5 times steeper color gradient than the local ones. Our results indicate that (i) more than a half of relatively massive disk-like galaxies at $z \sim 1$ are in violent star formation epochs observed as LIRGs, and also (ii) most of those LIRGs are constructing their fundamental disk structure vigorously. The high SFR density in the universe at $z \sim 1$ may be dominated by such star formation in disk region in massive galaxies.

Key words: galaxies: spiral — galaxies: starburst — galaxies: structure — infrared: galaxies

1. Introduction

It has been well known that the star formation rate (SFR) density of the universe (cosmic SFR density) increases by an order of magnitude from the present to $z \sim 1$ (Lilly et al. 1995; Madau et al. 1996; Hogg et al. 1998; Flores et al. 1999; Haarsma et al. 2000; Hopkins 2004; Hopkins & Beacom 2006). What kind of galaxies are contributing to such a large cosmic SFR density at $z \sim 1$ is still an open question.

In recent years with the *Spitzer Space Telescope*, many studies focusing on understanding the properties of distant star-forming galaxies have been conducted. The cosmic SFR densities at high redshifts are dominated by infrared bright galaxies, especially Luminous Infrared (IR) Galaxies (LIRGs) which have IR (8–1000 μm) luminosities, L_{IR} , of $10^{11}-10^{12} L_\odot$ (Flores et al. 1999; Takeuchi et al. 2005; Le Floc'h et al. 2005; Caputi et al. 2007; Pérez-González et al. 2008a; Magnelli et al. 2009; see

Sanders & Mirabel 1996 for a review on LIRGs). Their luminous IR emission is thermal dust emission in the mid-IR (MIR) to far-IR (FIR) wavelength caused by absorbing UV photons from intensive star formation and/or luminous active galactic nuclei (AGNs). IR luminosity of $10^{11} L_\odot$ corresponds to the SFR of $\sim 15 M_\odot \text{ yr}^{-1}$ (Kennicutt 1998), which is several to ten times larger than that of local normal galaxies (Brinchmann et al. 2004). Although in the local universe LIRGs are rare and have only $\sim 5\%$ contribution to the IR luminosity density, the number density of LIRGs increases with redshift, and 70% of the IR luminosity density is in LIRGs at $z \sim 0.7$ (Le Floc'h et al. 2005). It is important to understand triggering processes of the LIRGs to unveil the physical cause of the evolution of the cosmic SFR densities.

In the local universe, most of LIRGs show irregular morphologies, indicating galaxy-galaxy interaction (Sanders & Mirabel 1996; Sanders & Ishida 2004). Even among the LIRGs which have spiral morphology apparently, a

significant fraction of them shows bar structure (Wang et al. 2006). Such morphological properties indicate that gas is pushed into the nuclear region and nuclear starburst is triggered.

On the contrary, at high redshifts ($0.7 \lesssim z \lesssim 1$), the *Hubble Space Telescope* (*HST*) imagings show that most of LIRGs have spiral (or late-type) morphology without any clear sign of merging and/or interaction (Zheng et al. 2004; Bell et al. 2005; Melbourne et al. 2005; Lotz et al. 2008). Those galaxies also have no bar structure (Zheng et al. 2005). Moreover, in the last couple of years, some studies dedicated on MIR spectra of such distant LIRGs found their spectral shape indicates cool dust temperature similar to local spiral galaxies with lower IR luminosity ($L_{\text{IR}} < 10^{10.5} L_{\odot}$) (Zheng et al. 2007; Symeonidis et al. 2009; Seymour et al. 2010). More recently, Takagi et al. (2010) reported that most of polycyclic aromatic hydrocarbon (PAH)-selected galaxies with $L_{\text{IR}} > 10^{11} L_{\odot}$ at $z \sim 1$ show PAH-to-total IR luminosity ratio similar to that of less luminous starburst galaxies using an AKARI multi-wavelength MIR photometry. Those distant LIRGs show similar properties to local massive spiral galaxies except for their high IR luminosities.

Previous morphological studies of LIRGs at high redshifts were conducted in the rest-frame optical range. However, the high IR luminosity of LIRGs indicates the presence of a large amount of dust, and then morphological analysis in Near-IR (NIR) range less affected by dust-extinction is necessary to examine existence of dust-obscured structures such as nuclear starburst seen in local LIRGs or bars invisible in optical. NIR wavelength is also suitable to reveal the distribution of old stellar populations which dominate stellar mass of galaxies. As a pioneering study in NIR, Melbourne et al. (2008) carried out targeted observations of 15 LIRGs at $0.4 \lesssim z \lesssim 1.2$ with Adaptive Optics (AO) in the *K*-band, and evaluated their morphologies visually. It was found that two thirds of the LIRGs look disky apparently while major mergers are $\sim 30\%$ at a maximum. They also found that only one LIRG has a clear bar structure. The distant LIRGs are different from local LIRGs in morphology, and star formation in the distant LIRGs seems to be smoothly distributed in their disk.

However, the morphological study by Melbourne et al. (2008) is based on the visual classification. Further NIR morphological studies with quantitative evaluation are necessary. In addition, although they observed normal galaxies (non-LIRGs) at the similar redshifts, it is still crucial to locate LIRGs in field galaxies in the same redshift range.

In this paper, we construct a stellar mass- and volume-limited, NIR morphological catalog of galaxies at $z \sim 1$ independent of IR luminosity using deep *K_s*-band data, and locate LIRGs among $z \sim 1$ galaxies. We evaluate the galaxy morphology quantitatively using two-dimensional light profile in both *K_s*- (rest-frame *J*-) and optical (rest-frame *U*- and *V*-) bands. Comparing the rest-frame NIR and UV-to-optical morphologies, we discuss distributions of old stellar population and currently star-forming re-

gion in the high redshift LIRGs and non-LIRG galaxies. Throughout this paper, we use a Λ -CDM cosmology with $\Omega_m = 0.3$, $\Omega_{\Lambda} = 0.7$, and $H_0 = 70 \text{ km s}^{-1} \text{ Mpc}^{-1}$. In this cosmology, 1 arcsec corresponds to 8.01 kpc at $z = 1$. We refer *HST*/Advanced Camera for Surveys (ACS) filters F435W, F606W, F775W, and F850LP as *B*₄₃₅, *V*₆₀₆, *i*₇₇₅, and *z*₈₅₀-bands, respectively.

2. Sample of $z \sim 1$ Galaxies

2.1. *K_s*-selected stellar mass catalog from MODS Deep Data

We construct a stellar mass-limited $z \sim 1$ galaxy sample using the *deep* catalog of Kajisawa et al. (2009, hereafter K09). The catalog contains 3203 *K_s*(Vega) < 24 mag galaxies in 28 arcmin² from MOIRCS (Multi-Object InfraRed Camera and Spectrograph, Suzuki et al. 2008) Deep Survey (MODS) ultra-deep image obtained with MOIRCS attached to the Subaru Telescope (Kajisawa et al. 2006). It covers a part of the Great Observatories Origins Deep Survey North (GOODS-N, Giavalisco et al. 2004) field including Hubble Deep Field North region (HDF-N). Utilizing publicly available multi-wavelength (*U B*₄₃₅ *V*₆₀₆ *i*₇₇₅ *z*₈₅₀ *J H K_s*, 3.6 μ m, 4.5 μ m, and 5.8 μ m) data and spectroscopic redshift (z_{spec}) catalogs in the GOODS-N field, K09 constructed a catalog of redshift and stellar mass for the *K_s*-selected sample. The redshifts and stellar masses were estimated by fitting model spectral energy distributions (SEDs) obtained from several population synthesis models to the SEDs of the sample. The Salpeter Initial Mass Function (IMF) in stellar mass range of 0.1 – 100 M_{\odot} (Salpeter 1955) is assumed in the SED fittings. In this paper, we adopt the photometric redshifts (z_{phot}) and stellar masses (M_s) obtained with GALAXEV population synthesis model (Bruzual & Charlot 2003). The comparison between the photometric and spectroscopic redshifts of the galaxies which have the spectroscopic data shows that the photometric redshift estimates have a good accuracy with median and standard deviation of $\delta z \equiv (z_{\text{phot}} - z_{\text{spec}})/(1 + z_{\text{spec}})$ of -0.002 and 0.072 and the fraction of the catastrophic failure ($\delta z > 0.5$) of 4.2% for galaxies with $z_{\text{spec}} = 0.8$ –1.2. Note that the photometric redshifts are used only for galaxies with no spectroscopic identifications in order to maximize the reliability of the redshift catalog. The stellar masses were calculated using the best-fit stellar mass-to-luminosity (M_s/L) ratio in the observed *K_s*-band. Typical uncertainties of the stellar masses estimated from the probability distributions in the SED fitting (Figure 2 in K09) show that the stellar mass errors at $z < 1.5$ are less than 0.1 and 0.05 dex for stellar masses $M_s > 10^{10} M_{\odot}$ and $M_s > 10^{11} M_{\odot}$, respectively. Those errors include the uncertainty of the photometric redshift for galaxies with no spectroscopic redshift. It should be mentioned that systematic and random uncertainties (typically 0.2 dex) associated with stellar population models and IMFs are not included in these values.

Figure 1(a) shows the stellar masses of galaxies in the MODS deep region at $z = 0.6$ –1.4. The MODS stellar

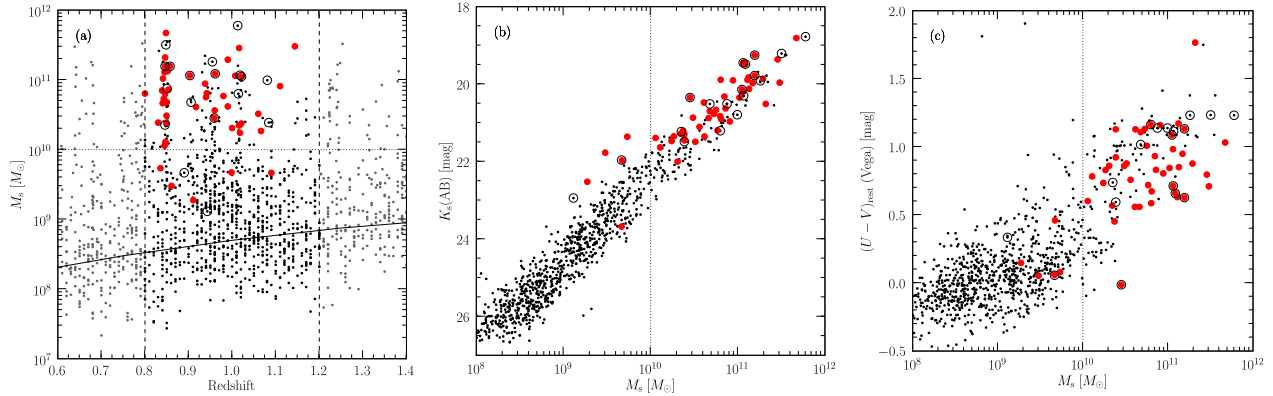


Fig. 1. Galaxies around $z = 1$ in the MODS deep region. (a) Stellar mass distribution of galaxies at $z = 0.6$ – 1.4 . The *dashed* lines separate our $z \sim 1$ ($z = 0.8$ – 1.2) galaxies from the K_s -selected sample. The *solid* line indicates the stellar mass limit corresponding to $K_s(\text{Vega}) = 24$ mag (Kajisawa et al. 2009, K09). The *dotted* line indicates a stellar mass limit for our morphological sample selection ($M_s = 1 \times 10^{10} M_\odot$) defined in Section 4.1. Large *filled* circles (red) represent MIPS $24 \mu\text{m}$ -detected ($f_{24} \geq 80 \mu\text{Jy}$) sources. *Chandra* X-ray-detected sources are marked with large *open* circle. (b) Stellar masses and K_s magnitudes of galaxies at $z = 0.8$ – 1.2 . (c) Stellar masses and rest-frame $U - V$ colors of galaxies at $z = 0.8$ – 1.2 . In all panels, the uncertainties of the stellar mass estimates are less than 0.1 and 0.05 dex for galaxies with $M_s = 10^{10} - 10^{11} M_\odot$ and with $M_s > 10^{11} M_\odot$, respectively.

mass catalog is complete down to at least $M_s \sim 10^9 M_\odot$ at these redshifts (shown with the solid line in the figure). In this paper, we focus on galaxies at $0.8 \leq z \leq 1.2$, which are plotted with black dots in the figure. For those $z \sim 1$ galaxies, we plot the distributions of the K_s magnitudes and the rest-frame $U - V$ colors as a function of stellar mass in Figure 1(b) and (c), respectively. There is a tight correlation between K_s magnitudes and stellar masses. Later, we will limit the sample with $M_s \gtrsim 10^{10} M_\odot$ considering the K_s -band morphological analysis limit of $K_s(\text{AB}) \sim 22.5$ mag (see Section 3 for the detail). The galaxies in the stellar mass range are located in redder part of the bimodal distribution of the rest-frame $U - V$ color in this redshift range. At $z = 0.8$ – 1.2 , $\sim 80\%$ (60%) of the galaxies in the MODS with $M_s \geq 3 \times 10^{10} M_\odot$ ($M_s = 1 - 3 \times 10^{10} M_\odot$) and with no X-ray-detection (see Section 2.3 for identification of X-ray sources) have spectroscopic redshifts.

2.2. MIPS $24\mu\text{m}$ flux and IR luminosity of the $z \sim 1$ Galaxies

In order to estimate IR luminosities, we looked for a *Spitzer*/MIPS (Multiband Imaging Photometer for *Spitzer*) $24 \mu\text{m}$ source counterpart for each $z \sim 1$ galaxy. The MIPS $24 \mu\text{m}$ source catalog provided by the GOODS team (M. Dickinson et al. in preparation; R. Chary et al. in preparation) contains sources with a $24 \mu\text{m}$ flux density (f_{24}) larger than $80 \mu\text{Jy}$ with 80% completeness. The catalog provides not only coordinates of the $24 \mu\text{m}$ sources themselves but also those of the IRAC counterparts if exists. We used the coordinates of the IRAC counterparts if available for the search. We identified 48 $24 \mu\text{m}$ counterparts in total for 808 galaxies with $K_s(\text{Vega}) < 24$ mag and $0.8 \leq z \leq 1.2$. In Figure 1, the $24 \mu\text{m}$ -detected sources are marked with large *filled* circles (red). Most of them have $K_s(\text{AB}) < 22$ mag, $M_s > 10^{10} M_\odot$, and bluer col-

ors in the rest-frame $U - V$ than the $24 \mu\text{m}$ -undetected galaxies in the same stellar mass range.

Among the K_s -selected galaxies with no $24 \mu\text{m}$ detection, we examine 112 galaxies with $M_s \geq 1 \times 10^{10} M_\odot$ (in our final sample defined in Section 4.1) on the MIPS $24 \mu\text{m}$ image (version 0.3) visually in order to estimate how many galaxies would be missed in the $24 \mu\text{m}$ catalog by confusion effect. We find that 12 out of 112 galaxies are located near bright $24 \mu\text{m}$ sources, and two of them have $M_s \geq 3 \times 10^{10} M_\odot$. If those 12 galaxies have a $24 \mu\text{m}$ flux larger than $80 \mu\text{Jy}$, the fraction of $24 \mu\text{m}$ -detected galaxies in our final sample will increase about 3% (13%) at $M_s \geq 3 \times 10^{10} (= 1 - 3 \times 10^{10}) M_\odot$.

For the $24 \mu\text{m}$ -detected galaxies, we estimate their bolometric IR luminosities L_{IR} (defined as $L_{\text{IR}} = L[8 - 1000 \mu\text{m}]$) from the observed $24 \mu\text{m}$ fluxes. Local IR-luminous ($L_{\text{IR}} > 10^{10} L_\odot$) galaxies show a tight correlation between $12 \mu\text{m}$ flux and L_{IR} estimated from 12, 25, 60 and $100 \mu\text{m}$ MIR flux densities with a scatter of ~ 0.15 dex (Chary & Elbaz 2001). Following their prescription, we convert the $24 \mu\text{m}$ fluxes (in μJy) of our $z \sim 1$ galaxies to the rest-frame $12 \mu\text{m}$ luminosities, and then compute their bolometric IR luminosities in solar luminosity as follows:

$$\nu_e S_{\nu_e}(12 \mu\text{m}) = \nu_o f_{24} \times 4\pi D_L(z)^2, \quad (1)$$

$$L_{\text{IR}} = 0.89_{-0.27}^{+0.38} \times [\nu_e S_{\nu_e}(12 \mu\text{m})]^{1.094}, \quad (2)$$

where D_L is the luminosity distance corresponding to the redshift z , ν_o is the observed frequency corresponding to the wavelength $\lambda = 24 \mu\text{m}$, and ν_e is the rest-frame frequency corresponding to the redshift z . The symbol S_ν is the monochromatic flux at a frequency ν expressed in $\text{erg s}^{-1} \text{Hz}^{-1}$. We need to note that the IR luminosity estimated using the rest-frame $12 \mu\text{m}$ flux density has an uncertainty of ~ 0.3 dex due to the uncertainty of the shapes of the IR SED (see Le Floch et al. 2005; Marcillac et al. 2006).

The 24 μm flux density limit of $f_{24} = 80 \mu\text{Jy}$ corresponds to the IR luminosity L_{IR} of 0.6×10^{11} , 1.1×10^{11} and $2.1 \times 10^{11} L_{\odot}$, and SFR of ~ 10 , 15, and $35 M_{\odot} \text{ yr}^{-1}$ at $z = 0.8$, 1.0 and 1.2, respectively. In this paper, we regard all the 24 μm -detected ($f_{24} \geq 80 \mu\text{Jy}$) galaxies as LIRGs while 24 μm -undetected ($f_{24} < 80 \mu\text{Jy}$) galaxies as non-LIRGs. We need to note that the LIRG identification is incomplete at $z = 1.0$ – 1.2 in the strict definition of LIRGs with $L_{\text{IR}} = 10^{11}$ – $10^{12} L_{\odot}$.

2.3. Identifying Chandra X-ray Sources

A part of the $z \sim 1$ galaxies is also detected in X-ray; 18 out of 808 galaxies with $K_s < 24 \text{ mag}$ and $0.8 \leq z \leq 1.2$ are detected in X-ray source catalog from the *Chandra* X-ray Observatory deep survey image (Alexander et al. 2003). In Figure 1, those X-ray-detected sources are marked with open circles. We checked those sources in the ACS z_{850} -band image, and all but one source are extended.

The evaluation of morphologies of those galaxies may be affected by bright point source of type I AGN. Also, if the SED of a galaxy is strongly contaminated by an AGN, no reliable stellar mass could be obtained without considering the effect of AGNs in the SED fitting. Moreover, MIR fluxes could not be a good indicator of SFR if their MIR radiations are mainly powered by UV radiation from AGNs. We will indicate those X-ray-detected galaxies with different symbols to the others in later figures, and exclude from the statistics.

3. Morphological Analysis

3.1. Sérsic profile fitting: Method

We evaluate the rest-frame NIR morphologies of the $z \sim 1$ galaxies using the MODS K_s -band image which is constructed from good seeing images. The MODS deep K_s -band data consists of images with various seeing sizes, FWHMs of from $0''.4$ to $1''.2$. The image used in K09 was the deepest one created by combining images with the FWHM smaller than $0''.8$, which has a total integration time of ~ 28 hours, 3σ limiting magnitude of $K_s(\text{AB}) \sim 26.4 \text{ mag}$ for point sources, and FWHM of the PSF of $\sim 0''.46$. Here, for the morphological analysis, we use a *shallower* but *sharper* image constructed from images with the FWHM $< 0''.5$, which gives a total integration time of ~ 16 hours and 3σ limiting magnitude of $K_s(\text{AB}) \sim 26.0 \text{ mag}$ for a point source, and the final FWHM of $0''.40$, which corresponds to a physical scale of $\sim 3.2 \text{ kpc}$ at $z = 1$ in the cosmology we use in this paper.

In order to describe morphologies of the $z \sim 1$ galaxies, we use a single component Sérsic model (Sersic 1968; see also Graham & Driver 2005 for detail of the model). It describes the radial surface brightness profile of a galaxy by a function given by,

$$I(r) = I(r_e) \exp \left\{ -b_n \left[\left(\frac{r}{r_e} \right)^{1/n} - 1 \right] \right\}, \quad (3)$$

$$r = \left[(x - x_c)^2 + \left(\frac{y - y_c}{q} \right)^2 \right]^{1/2}, \quad (4)$$

where x and y are aligned with the semimajor and semiminor axes, r is the elliptical radial distance at a pixel (x, y) from the center of a source (x_c, y_c) , q is the axial ratio of the semiminor to the semimajor axis radius, r_e is the major axis half-light radius or effective radius which contains the half of the total flux, and n is the Sérsic index which determines how the light profile concentrates around the center and how the profile extends to the outskirts. The b_n is a normalization constant which is a function of n and is chosen so that r_e is equivalent to the half-light radius. The Sérsic model includes a wide range of profiles of local galaxies such as the exponential ($n = 1$) and de Vaucouleurs ($n = 4$) models. In fact, a tight correlation between n and Hubble T-type (T) is observed in the local universe (Ravindranath et al. 2004) and even at $z \lesssim 1$ (Pannella et al. 2006); on average, galaxies with $n < 2$ – 2.5 are mostly disk-like objects ($T \gtrsim 2$) while galaxies with $n > 2$ – 2.5 are mostly spheroids (elliptical and bulge-dominated galaxies; $T \lesssim 2$).

We use the two-dimensional surface-brightness profile fitting code, GALFIT ver.2.0.3c (Peng et al. 2002). GALFIT convolves a two-dimensional model profile with a point-spread function (PSF) defined by user, and minimizes χ^2 residuals between the model profile and a real galaxy profile with a Levenberg-Marquardt algorithm. In the χ^2 minimization, there are 7 free parameters: Sérsic parameters (n and r_e), total magnitude, semiminor-to-semimajor axial ratio q , position angle PA , and the center position (x_c, y_c) of a galaxy. Initial guesses for those parameters except for n (being set to 1.5) were estimated based on the output parameters from SExtractor (Bertin & Arnouts 1996) object detection code. To estimate χ^2 correctly, we take into account the pixel-to-pixel signal-to-noise ratio. The dominant source of noise for NIR imaging data is Poissonian noise from sky background radiation. Therefore we use the square root of the exposure map as pixel-to-pixel weights in the χ^2 minimization.

The PSF used in this paper is obtained by stacking about 10 spectroscopically-identified isolated stars. The stars are distributed over the K_s -band image, and their FWHMs are quite uniform ($3.42 \pm 0.02 \text{ pixel}$). We therefore ignored the dependence on the position in the image, and combined all the stars to create a composite PSF, which is applied to all the $z \sim 1$ galaxies.

For a fitting region, one must have a sufficiently wide image size of a galaxy to cover the outskirts of the profile in the calculation. Following the galaxy two-dimensional profile fitting procedure used in the Galaxy Evolution from Morphology and SEDs (GEMS) survey (Häussler et al. 2007), we use an image stamp for each galaxy with a size (height and width) of 2.5 times the semimajor axial length of the Kron elliptical aperture derived from the SExtractor output which is expected to contain more than 90% of the total flux of the galaxy regardless of brightness (Kron 1980). Neighboring galaxies around

the galaxy of interest were masked and excluded from the fitting, or were fitted simultaneously if they are so close to the galaxy of interest. We determined whether a neighbor should be masked out or fitted simultaneously based on their Kron elliptical apertures same as in Häußler et al. (2007). First, the apertures are enlarged by increasing the semiminor and the semimajor axis radii by a factor of 1.5, and then if the neighbor’s extended aperture overlaps the extended aperture of the galaxy of interest, the neighbor is fitted simultaneously; otherwise, the neighbor is masked out with the extended aperture. Neighbors with $K_s(\text{AB}) > 22.5$ mag are masked out regardless of the overlap because the profile fitting for them would not be reliable (see the next subsection). Note that a difference in the treatment of neighbors (masked or fitted) has little effect on the fitting result for a galaxy of interest, except for galaxies with very bright neighbors, which suffer flux contamination from the neighbors and their fittings fail or derive obviously unreliable results with bright residuals.

3.2. Sérsic profile fitting: Simulation

To quantify how reliably we evaluate morphology of galaxies with the MODS K_s -band image, we perform a Monte Carlo simulation with ~ 1000 artificial galaxies. GALFIT is used to generate artificial galaxy images with parameters given randomly in the following ranges: $18 \leq K_s(\text{AB}) \leq 24$ mag, $0.3 \leq r_e \leq 25$ pixel (equivalent to $0.''035\text{--}2.''9$ or $0.3\text{--}23$ kpc at $z = 1$), $0.5 \leq n(K_s) \leq 10$, $0.1 \leq q \leq 0.9$, and $0 \leq PA \leq 180$ deg. Each artificial galaxy is convolved with the PSF used for the real galaxies, and is embedded randomly in the K_s -band image. SExtractor is used to detect them and measure apparent shapes, which are used as initial guesses for GALFIT in the same manner as for the real galaxies.

Using the number of galaxies detected among galaxies embedded, we first show detection completeness as a function of input magnitude and effective radius for low- $n_{\text{input}}(K_s)$ ($n_{\text{input}}[K_s] \leq 2.5$) sample and high- $n_{\text{input}}(K_s)$ ($n_{\text{input}}[K_s] > 2.5$) sample in Figure 2(a) and (b), respectively. Also shown in both panels is the distribution of the K_s magnitude (MAG_AUTO from SExtractor) and effective radius evaluated with GALFIT of the $z \sim 1$ galaxies with $M_s \geq 1 \times 10^{10} M_\odot$ according to $n(K_s)$. Although faint and large galaxies (located at top-right in Figure 2) can be missed at $K_s(\text{AB}) \geq 22.5$ mag in the low- $n(K_s)$ sample, all the detected $z \sim 1$ galaxies are located well below the detection limit.

Comparing input parameters with measured ones for the detected artificial galaxies, we estimate the uncertainty of the profile fitting parameters. For this analysis, we only select the artificial galaxies having measured K_s -band magnitudes and effective radii within 20% of those of the observed $z \sim 1$ galaxies (shown in Figure 2 with filled symbols). Figure 3 shows the differences between the input and measured parameters as a function of K_s input magnitude. There is no systematic offset in any parameters up to $K_{s,\text{input}}(\text{AB}) = 22.5$ mag. At $K_{s,\text{input}}(\text{AB}) \sim 22.5$ mag, we find that low- $n_{\text{input}}(K_s)$ galaxies tend to have $-1(\pm 34)\%$ lower Sérsic index, $0(\pm 9)\%$ lower size,

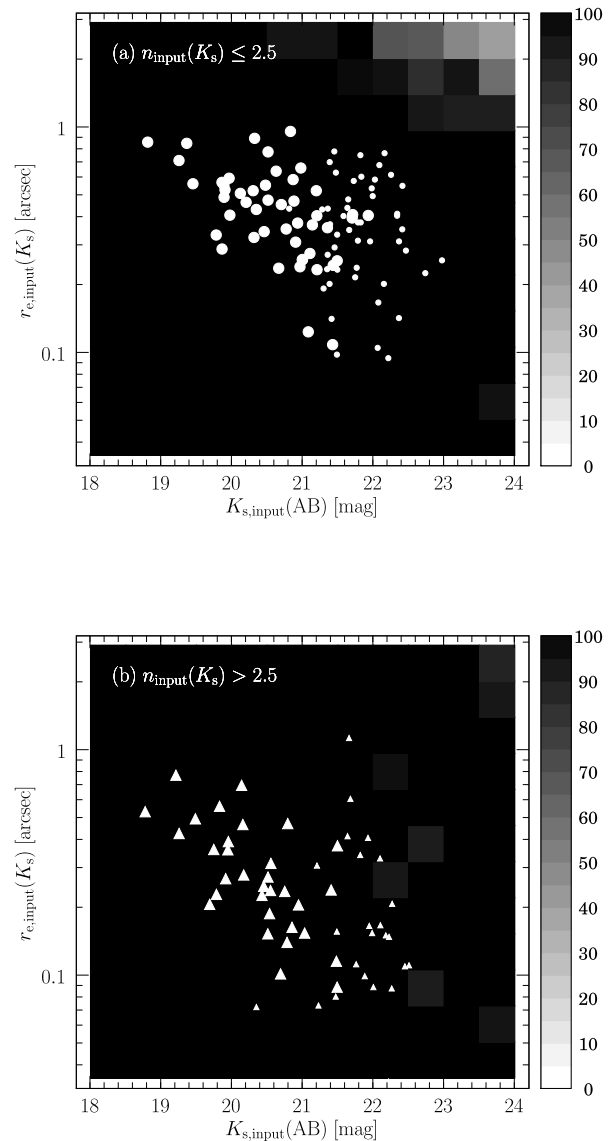


Fig. 2. Detection completeness map for galaxies in the MODS K_s -band image estimated from the artificial galaxy simulation. (a) The map for artificial galaxies with $n_{\text{input}}(K_s) \leq 2.5$. The grey-scale map indicates the simulation result. Overplotted large (small) *circles* show the observed effective radii and K_s magnitudes of the $z \sim 1$ galaxies with $M_s \geq 3 \times 10^{10} M_\odot$ ($M_s = 1\text{--}3 \times 10^{10} M_\odot$) and $n(K_s) \leq 2.5$ in the MODS. (b) Similar to the panel (a), but for galaxies with $n(K_s) > 2.5$.

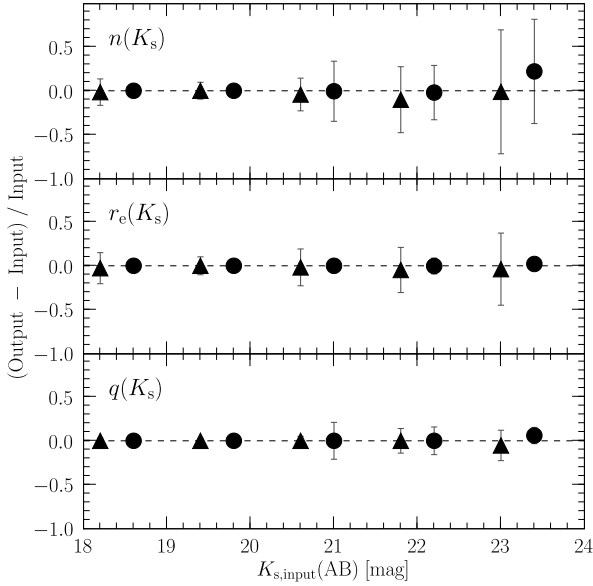


Fig. 3. Magnitude dependences of the difference between input and output structural parameters for artificial galaxies (circles for those with $n_{\text{input}}[K_s] \leq 2.5$ and triangles for those with $n_{\text{input}}[K_s] > 2.5$). From the *top* to *bottom* panel, the median difference and 1σ scatter are shown for Sérsic indices $n(K_s)$, effective radii $r_e(K_s)$, and axial ratios $q(K_s)$. Among the galaxies detected, we used only those with the similar K_s magnitude (± 0.2 mag) and the effective radius (80–120%) compared to the observed $z \sim 1$ galaxies.

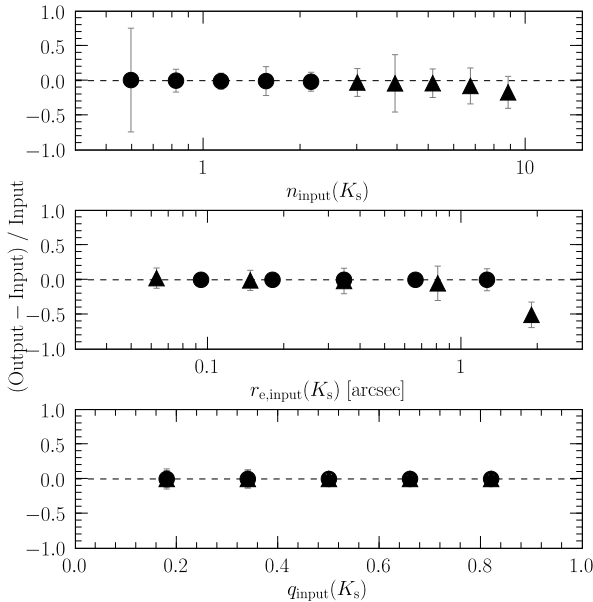


Fig. 4. Difference between input and output values for each structural parameter as a function of input value for artificial galaxies. From the *top* to *bottom* panel, the median difference and 1σ scatter are shown for Sérsic indices $n(K_s)$, effective radii $r_e(K_s)$, and axial ratios $q(K_s)$. The symbols are the same as in Figure 3. Among the galaxies used in Figure 3, we used only those with $K_{s,\text{input}}(\text{AB}) \leq 22.5$ mag.

and $1(\pm 14)\%$ larger axial ratio, and high- $n_{\text{input}}(K_s)$ galaxies tend to have $-3(\pm 45)\%$ lower Sérsic index, $-4(\pm 29)\%$ lower size, and $-5(\pm 16)\%$ lower axial ratio.

Finally, we examine differences between input and output values for each parameter as a function of input value of the galaxies with $K_s(\text{AB}) \leq 22.5$ mag, which are shown in Figure 4. We find no significant trend in each parameter for the low- $n_{\text{input}}(K_s)$ sample. On the contrary, for the high- $n_{\text{input}}(K_s)$ sample we find a systematic offset of $\Delta n/n \sim -15\%$ and $\Delta r_e/r_e \sim -10\%$ for galaxies with $n_{\text{input}}(K_s) \gtrsim 8$. Although those offsets less affect to our morphological separation criterion of $n(K_s) = 2.5$ (described in Section 4.1), we have to keep in mind the offset in size when we study the sizes of the high- $n(K_s)$ galaxies.

Based on the results of the simulation with artificial galaxies, we find that the morphological analysis using GALFIT with the MODS deep K_s -band image is reliable up to $K_s(\text{AB}) \sim 22.5$ mag. Therefore, in later sections we will limit our $z \sim 1$ morphological sample at the stellar mass of $M_s \sim 10^{10} M_\odot$ corresponding to that magnitude.

3.3. Non-parametric morphological analysis

We perform an another morphological analysis based on a non-parametric method: Concentration-Asymmetry (C - A) analysis (Abraham et al. 1994; Abraham et al. 1996; Conselice et al. 2000; Conselice 2003). Unlike GALFIT, the C - A analysis does not require information on the shape of the PSF and assumptions on the shape of the light profile. Therefore, we use this method in parallel with the Sérsic profile fitting.

The concentration index (C) is an indicator how the light profile of a galaxy concentrates around the center. The definition used in this paper is,

$$C = 5 \log_{10} \left(\frac{r_{80}}{r_{20}} \right), \quad (5)$$

where r_{80} and r_{20} are the radii which contain 80% and 20% of the total flux, respectively. The total flux is defined as MAG_AUTO derived from the SExtractor output. This parameter is related to n of Sérsic profile and there is certainly a correlation between these two parameters.

The asymmetry index (A) is an indicator how the two-dimensional light profile is disturbed, which is defined as,

$$A = \frac{1}{2} \left[\min \left(\frac{\sum |I_0 - I_{180}|}{\sum |I_0|} \right) - \min \left(\frac{\sum |B_0 - B_{180}|}{\sum |I_0|} \right) \right], \quad (6)$$

where I_0 and I_{180} are the intensity of each pixel of the image and of the image rotated by 180° around the galaxy centroid, respectively. The symbols B_0 and B_{180} have the similar definitions but for the background region. The A is defined as the minimum value with varying the position of the center of rotation around the original galaxy centroid. The summation taken in the area is defined using the Kron elliptical aperture used in Section 3.1. We found that the contribution of sky background, the term $\sum |B_0 - B_{180}|$, correlates well to the elliptical aperture size, and is less dependent on the position on the image. Therefore, we

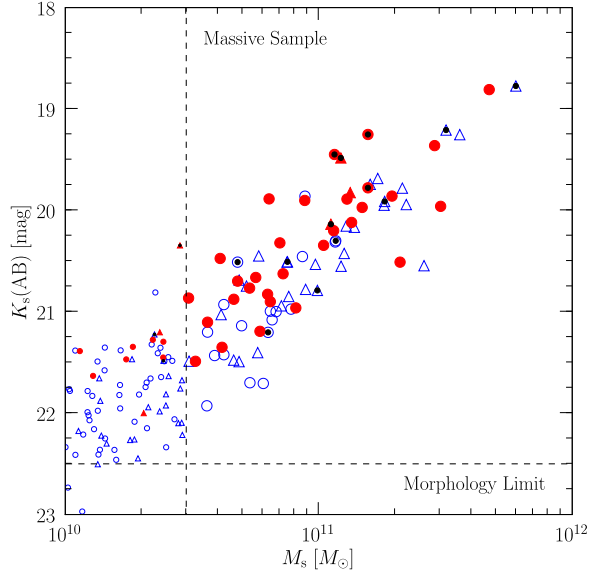


Fig. 5. K_s magnitude distribution of $z \sim 1$ galaxies as a function of stellar mass. The *filled* symbols show the LIRGs while *open* symbols show the non-LIRGs. The sample is divided by the Sérsic index: *circles* for low- $n(K_s)$ ($n[K_s] \leq 2.5$) galaxies and *triangles* for high- $n(K_s)$ ($n[K_s] > 2.5$) galaxies. The X-ray-detected sample is marked with black dots. The horizontal *dashed* line represents $K_s(\text{AB}) = 22.5$ mag, which indicates the limit of morphological analysis. This magnitude corresponds to the stellar mass of $\sim 1 \times 10^{10} M_\odot$ which is adopted as our stellar mass-limited morphological sample criterion. The vertical *dashed* line separates less massive ($M_s = 1-3 \times 10^{10} M_\odot$) and massive ($M_s \geq 3 \times 10^{10} M_\odot$) galaxies. The less massive galaxies are indicated with smaller symbols.

assume a universal background over the image and scale it according to the aperture size of galaxies.

4. Results

4.1. Rest-frame NIR morphologies of $z \sim 1$ LIRGs

The morphological simulation shows that the MODS K_s -band image allows us to evaluate a light profile of galaxies with $K_s(\text{AB}) \sim 22.5$ mag or brighter (Section 3.2). As seen in Figure 1(b), this K_s magnitude limit corresponds to $M_s \sim 10^{10} M_\odot$ at $z \sim 1$. We therefore apply a stellar mass cut of $M_s = 1 \times 10^{10} M_\odot$ to the $z \sim 1$ galaxy sample to define a morphological sample, which contains 139 galaxies in total. Considering the scatter in K_s magnitude at $M_s = 1 \times 10^{10} M_\odot$ (representing a variety of M_s/L), we also construct a more conservative morphological sample containing galaxies with $M_s \geq 3 \times 10^{10} M_\odot$, to which 67 out of 139 galaxies belongs. We refer the galaxies with $M_s \geq 3 \times 10^{10} M_\odot$ ($M_s = 1-3 \times 10^{10} M_\odot$) as massive (less massive) galaxies. Our morphological sample achieves high completeness thanks to the very deep imaging data; 100% and 96% for the massive and less massive sample, respectively. We summarize in Table 1 the numbers of the $z \sim 1$ galaxy morphological subsample in the MODS deep region for stellar mass cuts

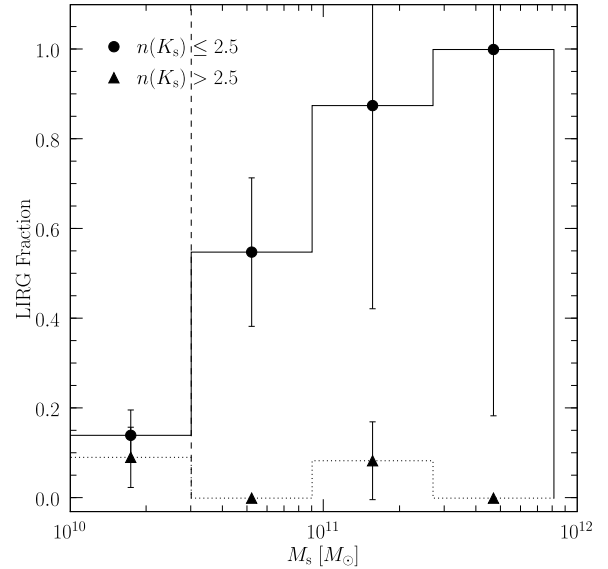


Fig. 6. Fraction of LIRGs (galaxies with $f_{24} \geq 80 \mu\text{Jy}$) as a function of stellar mass. The samples are split into two groups ($n[K_s] \leq 2.5$: *circles* and $n[K_s] > 2.5$: *triangles*). All the X-ray-detected galaxies are excluded. The error bars account for Poissonian errors only.

of $M_s = 1-3 \times 10^{10} M_\odot$ and $M_s \geq 3 \times 10^{10} M_\odot$. In the parentheses, the numbers of galaxies with spectroscopic redshift are shown. The spectroscopic redshifts are available for about 60% and 80% of less massive and massive galaxies, respectively. The uncertainty of the photometric redshift estimates of 0.072 (Section 2.1) brings about 1–2% uncertainties in physical size (R_e) estimates, which is sufficiently small for our study. In Appendices we show the properties and images used in this study for all the $z \sim 1$ sample.

Figure 5 summarizes the morphological evaluation for the $z \sim 1$ galaxies in the stellar mass– K_s magnitude diagram. The sample is divided by their IR luminosities (LIRGs and non-LIRGs) and Sérsic indices (less concentrated system: low- $n[K_s]$ and highly concentrated system: high- $n[K_s]$) in the figure. The X-ray-detected sample is marked with black dots. For $M_s < 3 \times 10^{10} M_\odot$, the sample is shown with small symbols. In addition to the fact that the LIRGs are popular at $M_s > 10^{10} M_\odot$ and bright in the K_s -band as already seen in Figure 1(b), most of them are classified in $n(K_s) \leq 2.5$. In Figure 6, these trends are shown quantitatively. Although with small sample size of the LIRGs at the most massive bin, the fraction of LIRGs in the sample increases with stellar mass, and most of them have $n(K_s) \leq 2.5$ while the LIRGs with $n(K_s) > 2.5$ are rare.

Figure 7(a) and (b) show the distribution of the structural parameters, the Sérsic indices $n(K_s)$ and the physical sizes (effective radii in kpc) along the semimajor axis $R_e(K_s)$, for galaxies with $M_s = 1-3 \times 10^{10} M_\odot$ and with $M_s \geq 3 \times 10^{10} M_\odot$, respectively. In each figure, the bottom and right panels show the respective distributions

Table 1. The number of sample galaxies in this paper*

	$M_s = 1-3 \times 10^{10} M_\odot$				$M_s \geq 3 \times 10^{10} M_\odot$			
	No X-ray		All		No X-ray		All	
LIRGs with $n[K_s] \leq 2.5$	7	(6)	7	(6)	27	(21)	30	(24)
LIRGs with $n[K_s] > 2.5$	2	(1)	3	(2)	1	(1)	3	(3)
Non-LIRGs with $n[K_s] \leq 2.5$	43	(29)	43	(29)	15	(8)	18	(11)
Non-LIRGs with $n[K_s] > 2.5$	20	(6)	22	(8)	24	(21)	29	(26)
Total	72	(42)	75	(45)	67	(51)	80	(64)

*In the parentheses, numbers of galaxies with spectroscopic redshift are given.

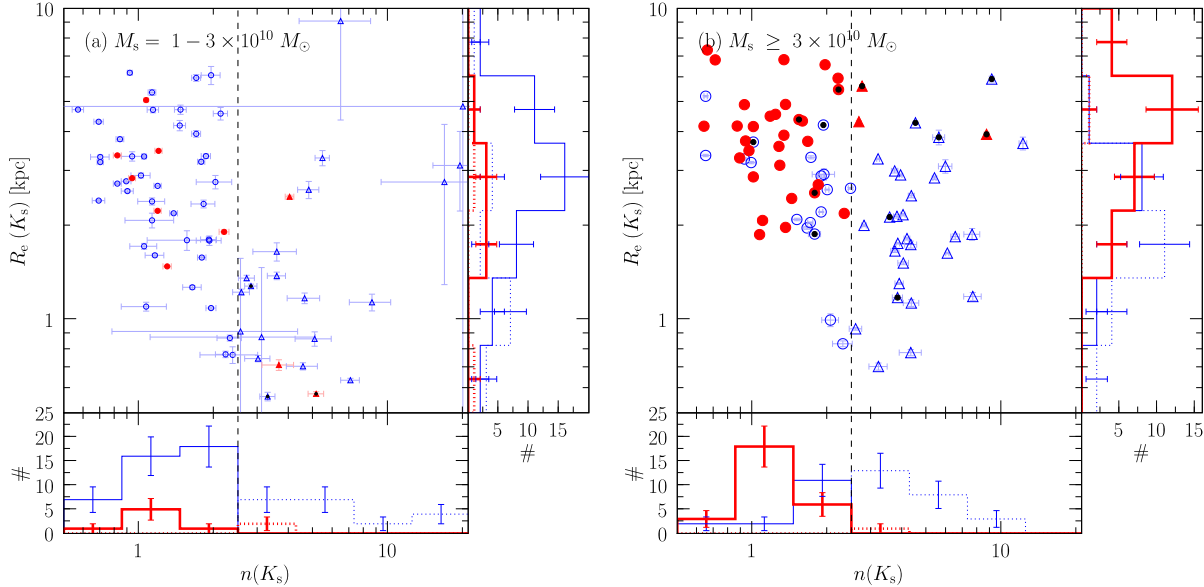


Fig. 7. Structural parameters (Sérsic indices and effective radii in physical scale along the semimajor axis) measured in the MODS deep K_s -band image for the $z \sim 1$ galaxies with (a) $M_s = 1-3 \times 10^{10} M_\odot$, and with (b) $M_s \geq 3 \times 10^{10} M_\odot$. The symbols are the same as in Figure 5. The error bars indicate the uncertainties of the fitting. The vertical dashed line separates less concentrated and highly concentrated systems ($n[K_s] \leq 2.5$ is considered as a less concentrated system). In each figure, the bottom and right panels show numbers of the samples at a given stellar mass range as a function of $n(K_s)$ and $R_e(K_s)$, respectively. Thick (thin) line corresponds to the numbers of the LIRGs (non-LIRGs), and solid (dotted) line corresponds to the numbers of the low- $n(K_s)$ (high- $n(K_s)$) sample. The error bars of the histograms account for Poissonian errors only. All the X-ray-detected galaxies are excluded from the counts.

of the parameters, where the X-ray-detected galaxies are excluded from the counts. Most of the LIRGs are well described with exponential disk-like profiles ($\langle n[K_s] \rangle \sim 1.2$). With our separation criterion of $n(K_s) = 2.5$ in the massive ($M_s \geq 3 \times 10^{10} M_\odot$) sample, 96% (27/[27+1]) of the LIRGs are classified in less concentrated (low- $n[K_s]$) system while only one galaxy ($\sim 3\%$) is in highly concentrated (high- $n[K_s]$), or bulge-dominated system. As seen in the bottom panel of Figure 7(b), the LIRGs have a skewed $n(K_s)$ -distribution where most of the LIRGs are distributed between $n(K_s) = 1-2$, and therefore the fraction is not changed significantly even if we use a different separation criterion; about 89% and 100% for the criterion $n(K_s) = 2.0$ and 3.0, respectively. Melbourne et al. (2008) reported the similar result to ours by AO-supported NIR observations that two thirds ($\sim 67\%$) of $z \sim 1$ LIRGs are disk-like galaxies according to their visual morphological classifications. Despite various differences between our

study and Melbourne et al. (2008) such as the spatial resolution of data (seeing-limited or AO-supported) or the morphological classification methods (based on the profile fitting or visual appearance), our study confirms quantitatively with larger number of sample that most of the $z \sim 1$ LIRGs have disk-like morphologies.

If we examine the fraction among the massive galaxies, we find that about 64% (27/[27+15]) of the low- $n(K_s)$ galaxies are LIRGs among the galaxies with $M_s \geq 3 \times 10^{10} M_\odot$. As seen in Figure 6 as well, the LIRG fraction in the low- $n(K_s)$ sample increases with stellar mass. At $z \sim 1$, the disk-like massive galaxies have surprisingly high fraction of LIRGs. In fact, the residual images after subtracting best fit Sérsic component show clear spiral structure for some of $z \sim 1$ galaxies.

As for the sizes, the right panel of Figure 7(b) shows that the LIRGs have larger $R_e(K_s)$ than the non-LIRGs on average. Comparing the low- $n(K_s)$ galaxies in between

LIRGs and non-LIRGs, a mean size and a sample scatter of the LIRGs is 3.8 ± 1.6 kpc while that of the non-LIRGs is 2.6 ± 1.0 kpc. The high- $n(K_s)$ non-LIRGs have a wide $R_e(K_s)$ -distribution and some of them have the sizes around 1 kpc. In the MODS deep data, a FWHM of the PSF is $0''.40$, which corresponds to $R_e(K_s) \sim 2$ kpc at $z = 1$. Since GALFIT takes into account the PSF in the profile fitting, sizes smaller than the PSF size can be evaluated in principle. However, the morphological analysis of those unresolved galaxies can be easily affected by what PSF (size and shape) is assumed in the fitting, and their resultant sizes would have larger uncertainties than the other larger galaxies. Therefore, we have to pay attention to those small ($R_e[K_s] \leq 2$ kpc) galaxies when discussing their sizes. However, for the LIRGs, most of them are much larger than the PSF size and their profiles must be derived reliably.

4.2. Rest-frame NIR Stellar Mass–Size Relation

We show the stellar mass–size distribution in the K_s -band (rest-frame J -band) in Figure 8(a) and (b) for the low- $n(K_s)$ and high- $n(K_s)$ sample, respectively. The sizes are shown as circularized effective radii, $R_{e,c} = R_e \times q^{1/2}$, where q is the intrinsic semiminor-to-semimajor axial ratio of the galaxy. The circularized method yields large difference in size between the LIRGs and non-LIRGs when compared to those derived from the semimajor axial radius of the galaxies which is shown in Figure 7. To compare those sizes with those of local galaxies, we construct a local galaxy catalog including spectroscopic redshifts, stellar masses, and Sérsic parameters using the NYU Value-Added Galaxy Catalog (VAGC; Blanton et al. 2005), which is based on the seventh release (DR7) of Sloan Digital Sky Survey (SDSS). The stellar masses are estimated from the fits to the broad-band (u , g , r , i , and z centered at 3540, 4770, 6230, 7630, and 9130 Å) photometry (Blanton & Roweis 2007) using a Chabrier IMF (Chabrier 2003) that we convert to the Salpeter IMF by adding a factor of 0.25 dex to them. The Sérsic parameters are measured in those five bands with a single component Sérsic model fitting (Blanton et al. 2003). Considering completeness of the SDSS data (Shen et al. 2003) and possible selection biases (Franx et al. 2008), we use the VAGC sample between redshifts of 0.05 and 0.07, the r -band apparent magnitudes of 15.0 and 17.7 mag, and the r -band surface brightnesses brighter than 23 mag arcsec $^{-2}$, which contains a sample of $\sim 4 \times 10^4$ galaxies in total. The criteria except for the redshift range affect weakly to the selection. In practice, we have analyzed a sample selected with only the redshift criterion ($0.05 \leq z \leq 0.07$), and found negligible change in the size distribution of the sample. The median redshift of the SDSS galaxies is 0.062 at which the SDSS z -band corresponds to the rest-frame ~ 8600 Å. We overplot in Figure 8 the effective radii measured in the SDSS z -band of the local galaxies as a function of stellar mass. The late- and early-type galaxies are separated at the Sérsic index in the z -band, $n(z) = 2.5$. We see for the both morphological types the LIRGs are comparable in size to or slightly (\sim

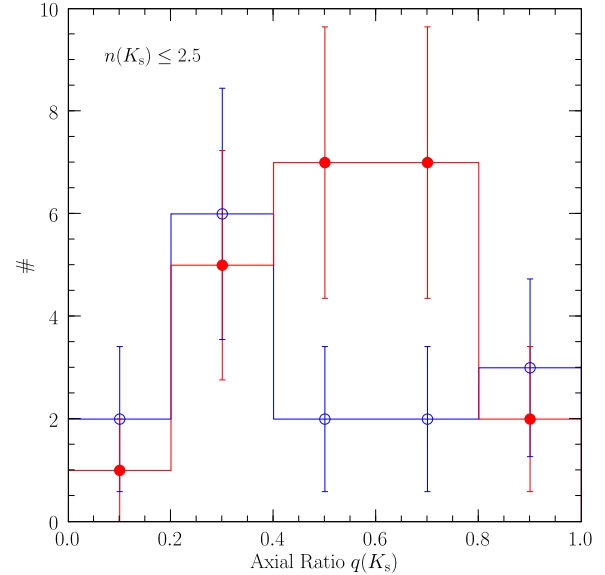


Fig. 9. The histogram of axial ratio measured in the K_s -band for the $z \sim 1$ galaxies with $n(K_s) \leq 2.5$ in the MODS. The symbols are the same as in Figure 5. Only the galaxies with $M_s = 3\text{--}15 \times 10^{10} M_\odot$ are included, and the X-ray-detected galaxies are excluded. The error bars account for Poissonian errors only.

20% at a maximum) smaller than the local galaxies while the non-LIRGs are significantly (30–70%) smaller than both the $z \sim 1$ LIRGs and the local galaxies. In particular, about a half of the low- $n(K_s)$ LIRGs have comparable sizes to the local disk-like galaxies. In the local universe, a size dependence on the measured wavelength, namely a color gradient, between 11000 Å and 8600 Å is known to be only a few per cent (smaller in redder band) for both disk-like galaxies (de Jong 1996; Barden et al. 2005) and early-type galaxies (McIntosh et al. 2005). Even if we take into account this color gradient to estimate sizes of the local galaxies at $\lambda = 11000$ Å, our result would be unchanged.

The trend that the non-LIRGs are further apart from the local relation compared to the LIRGs is in good agreement with a study by Pérez-González et al. (2008b), who used deeper MIPS 24 μm image than ours and found that 24 μm -undetected ($f_{24} < 15 \mu\text{Jy}$) sources are smaller than other 24 μm sources for galaxies with $M_s > 10^{11} M_\odot$. We find that the larger difference in circularized size between the low- $n(K_s)$ LIRGs and low- $n(K_s)$ non-LIRGs is partly caused by the fact that those two groups have different distributions of axial ratio, which is shown in Figure 9. For a comparison of axial ratio, here we limit the sample within $M_s = 3\text{--}15 \times 10^{10} M_\odot$ which is the stellar mass range of the low- $n(K_s)$ non-LIRGs. A median axial ratio and a scatter for the LIRGs and non-LIRGs are 0.57 ± 0.21 and 0.38 ± 0.26 , respectively. Taking into account the difference in axial ratio, we replot the stellar mass–size relation at $z \sim 1$ using not the circularized sizes ($R_{e,c}$) but the semimajor axis sizes (R_e) in Figure 10. The LIRGs are

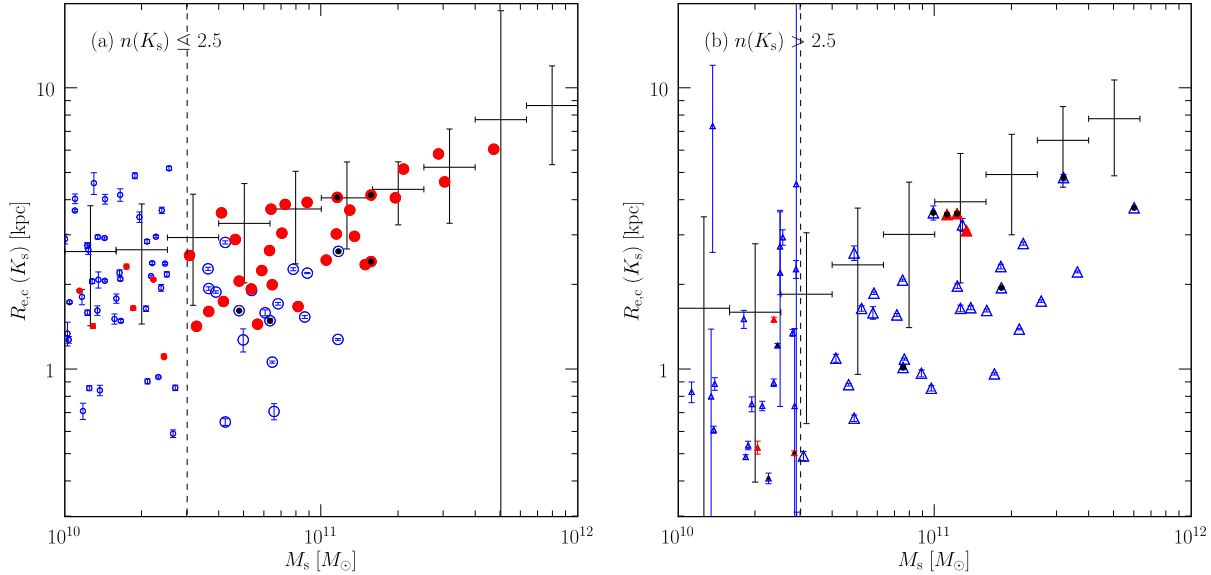


Fig. 8. The circularized effective radius of the $z \sim 1$ galaxies with (a) $n(K_s) \leq 2.5$, and with (b) $n(K_s) > 2.5$ as a function of stellar mass. The symbols are the same as Figure 5. The error bars indicate the uncertainties of the fitting. The median and dispersion of the distribution of effective radius in z -band of local late-type ($n[z] \leq 2.5$) and early-type ($n[z] > 2.5$) galaxies (redshifts of ~ 0.062) derived from VAGC (Blanton et al. 2005) are overplotted as a function of stellar mass.

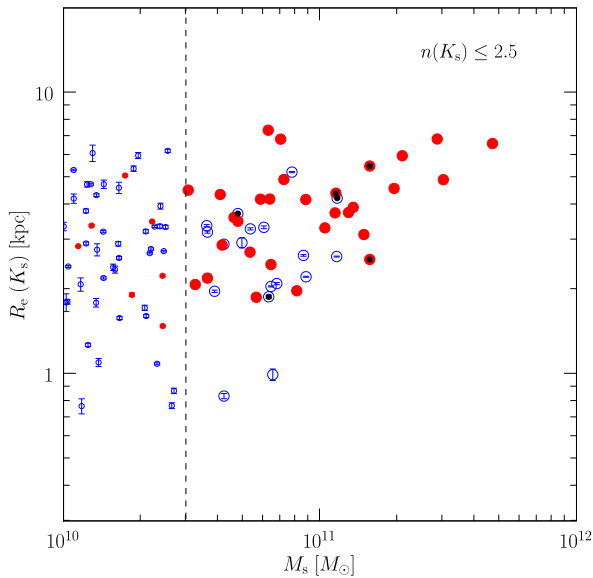


Fig. 10. Similar to Figure 8(a) but the sizes are described as the effective radii measured along to the semimajor axis. The symbols are the same as in Figure 5. The error bars indicate the uncertainties of the fitting.

still larger than the non-LIRGs although the size difference between the LIRGs and non-LIRGs seen in Figure 8 becomes small.

Although some of the low- $n(K_s)$ non-LIRGs with low axial ratio ($q[K_s] < 0.4$) show redder $U - V$ colors than the low- $n(K_s)$ LIRGs which may be caused by their high inclination angles, we cannot investigate further the cause of the different $q(K_s)$ distributions considering the small sample size.

4.3. Concentration-Asymmetry indices

Figure 11 shows the result of Concentration-Asymmetry (C - A) measurement in the MODS deep K_s -band image of the $z \sim 1$ galaxies. Since the wavelength in which the indices measured is longer than that in previous (optical) studies, separation criteria of morphological type of galaxies on the C - A plane established by those studies (e.g., Conselice 2003) are not applicable on our (rest-frame J -band) C - A plane. Therefore, it is difficult to interpret absolute values of C and A measured in the K_s -band. Nonetheless, relative comparison of those values within the $z \sim 1$ sample (LIRGs versus non-LIRGs or low- $n(K_s)$ versus high- $n(K_s)$ sample) is meaningful to investigate the difference between the populations. Figure 11 shows the consistent distribution of morphologies with the result of the GALFIT analysis. Most of the LIRGs have low $C(K_s)$ compared to the non-LIRGs which are distributed widely in $C(K_s)$. That is the similar trend as seen in the classification with Sérsic index. We actually find that $C(K_s)$ correlates with $n(K_s)$ well in our sample.

A part of galaxies show larger $A(K_s)$ than the others. At the index $A(K_s) > 0.1$, there are 12 galaxies ($\sim 15\%$ of the total) for the massive sample. High $A(K_s)$ indices

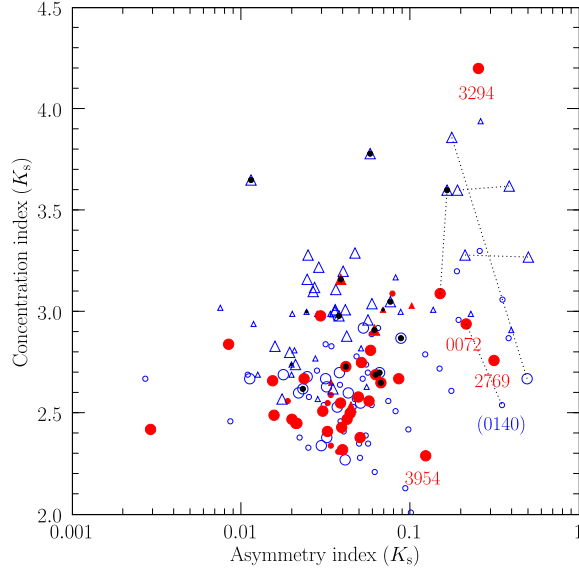


Fig. 11. Asymmetry (A) and Concentration (C) indices of the $z \sim 1$ galaxies measured in the MODS deep K_s -band image. The symbols are the same as in Figure 5. The *dotted* lines connect probable physically-interacting pairs in the massive ($M_s \geq 3 \times 10^{10} M_\odot$) sample where two galaxies have close spectroscopic redshifts as well as being located closely (≤ 1.5 arcsec) in the K_s -band image. The galaxy ID:0072 has a companion (ID:0140) which is in the less massive ($M_s = 1\text{--}3 \times 10^{10} M_\odot$) sample. The galaxy ID:2769 ($z_{\text{phot}} = 0.98$) shows a high A due to the existence of a companion (ID:2722) which have a spectroscopic redshift of 0.581 (not shown in the figure); this pair is just due to a random projection. The galaxy ID:3294 is located close to very bright source. The galaxy ID:3954 is located close to the edge of the image.

of two out of 12 galaxies are partly affected by nearby bright source (ID:3294) or by located near the edge of the image (ID:3954). The remaining 10 galaxies have a companion very close (≤ 1.5 arcsec or ≤ 12 kpc in projected distances) to themselves. Among the 5 pairs, 4 pairs have almost the same spectroscopic redshift to each other, which means that they can be physically interacting, not a random projection. Those interacting pairs are connected with *dotted* lines in Figure 11. The remaining one pair might be just due to the projection; the galaxy ID:2769 have a photometric redshift of 0.98 while the companion have a spectroscopic redshift of 0.581. Therefore, highly asymmetric features observed in the $z \sim 1$ sample are thought to be induced mainly by strong interaction (i.e., major-merging events). IR luminosities (an indicator of dusty star formation activity) are shown as a function of the asymmetry indices in Figure 12. The median and 1- σ scatter of the index $A(K_s)$ for the LIRGs and the non-LIRGs are 0.039 ± 0.076 and 0.034 ± 0.105 , respectively. We find no correlation between star formation and NIR asymmetry property.

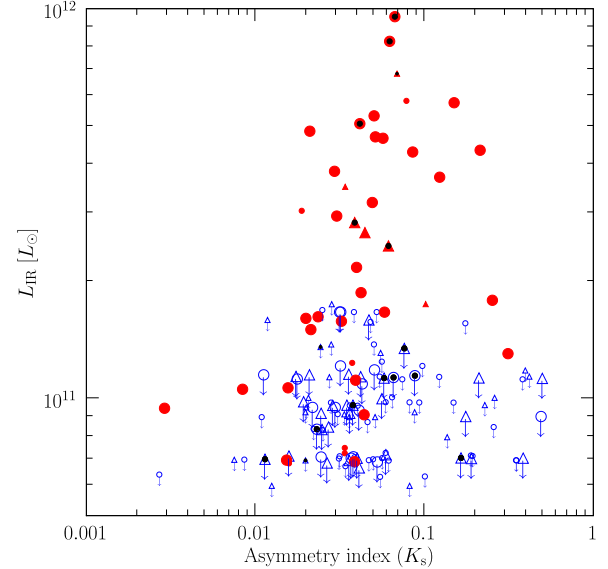


Fig. 12. IR luminosities of the $z \sim 1$ galaxies in the MODS as a function of Asymmetry index measured in the K_s -band. The symbols are the same as in Figure 5. The non-LIRGs (i.e., $24 \mu\text{m}$ -undetected galaxies) are also marked with down-pointing arrows as their upper limits of L_{IR} corresponding to $f_{24} = 80 \mu\text{Jy}$ at their redshifts.

5. Discussion

As seen in Section 2.2, our sample contains majority of $z \sim 1$ LIRGs which are thought to be a major star-forming population at that epoch. Quantitative morphological analysis reveals that those LIRGs show low- $n(K_s)$ (disk-like) structure in the NIR. This is consistent with the result of the AO-supported study in the K -band of Melbourne et al. (2008). Also, the low- $n(K_s)$ LIRGs consist of more than a half of the whole low- $n(K_s)$ galaxies at $z \sim 1$ above $M_s \geq 3 \times 10^{10} M_\odot$. Those observational evidences indicate that the star formation at $z \sim 1$ is mainly occurred in relatively massive disk-like galaxies, and that those star-forming massive disk-like galaxies are popular at $z \sim 1$. In addition, the fact that the low- $n(K_s)$ galaxies in our sample does not show any correlation between the asymmetry and the IR luminosity except for a few close pairs indicates that the star formation is not triggered mainly by early-stage major-merging events which disturb the NIR morphology strongly while it is still possible that some of the LIRGs are in late stage of interaction. As a next step, we investigate rest-frame UV-to-optical morphologies of the low- $n(K_s)$ galaxies to understand how the star formation is occurred in the massive disk-like galaxies.

We use the ACS V_{606} - and z_{850} -bands (rest-frame U - and B -bands) images and the source catalogs version 2.0 provided by the GOODS project to examine the distribution of star-forming regions in the $z \sim 1$ galaxies, and to compare them with those of local disk-like galaxies. First, we find a z_{850} -band counterpart for all the $z \sim 1$

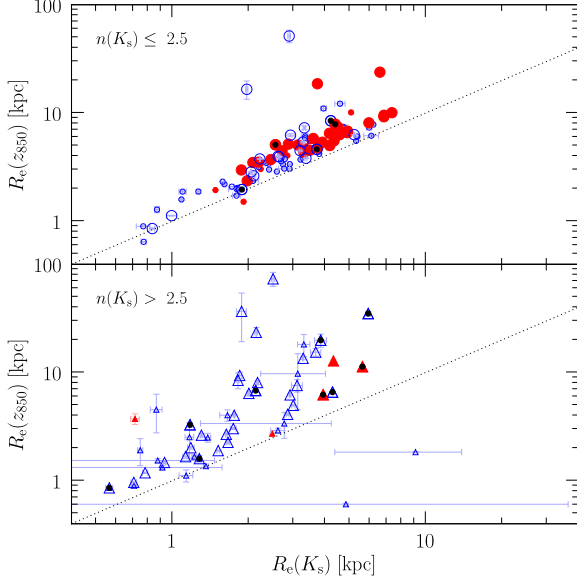


Fig. 13. The comparison of effective radii measured in the K_s - and z_{850} -band. The symbols are the same as in Figure 5. The dotted diagonal indicates where the parameters derived in the z_{850} -band are equal to those in the K_s -band. The error bars indicate the uncertainties of the fitting.

(K_s -selected) galaxies. For galaxies with multiple z_{850} -band counterparts, we select the closest one as a counterpart. Two of the 139 $z \sim 1$ galaxies (ID=3294, 3844) have no z_{850} -band counterparts. Both of them are close to a bright star, which may have made the z_{850} -band source detection failed in those region. We do not try to tune detection parameters to detect them, but remove them from the current discussion. Then, we perform the profile fitting for the z_{850} -band counterparts using GALFIT in a similar manner as for the K_s -band galaxies except for fitting the background sky level simultaneously in the z_{850} -band image. Similar to the K_s -band morphological analysis, we use the SExtractor outputs as initial guesses except for n which is set to 1.5. We use a weight map produced by the GOODS team for the signal-to-noise per pixel. We create a PSF image for each ACS tile by stacking spectroscopically-identified, unsaturated stars in the tile. We confirm that even if we smooth and resample the z_{850} -band image to match the image qualities (i.e., pixel scale and PSF size) to those of the K_s -band image, the fitting results are little changed in a statistical sense in comparison with results evaluated with the original z_{850} -band image. Then, we evaluate the V_{606} -band morphologies of the galaxies in the similar manner. Among the z_{850} -band structural parameters, the semimajor, semiminor axial radius, the axial ratio, and the position angle are used as initial guesses for GALFIT. The position x , y are fixed at those in the z_{850} -band. The initial guess of the total magnitude is obtained from the GOODS-N public catalog.

Figure 13 shows the comparison of the effective radii along the semimajor axis measured in the K_s -band and

z_{850} -band. We mention that there is no significant difference in Sérsic index and axial ratio between the rest-frame UV-to-optical and NIR bands. The $R_e(K_s)$ is systematically smaller than the $R_e(z_{850})$ irrespective of the IR luminosity; a mean size and an uncertainty of the mean of $R_e(K_s)/R_e(z_{850}) \sim 0.65 \pm 0.01$ and 0.44 ± 0.01 for the low- and high- $n(K_s)$ massive sample, respectively. The difference between rest-frame J -band and B -band sizes found in our $z \sim 1$ sample is a factor of 3–5 larger than that for local galaxies. Similar trend of larger color gradient of $z \sim 1$ galaxies was reported by Trujillo et al. (2007). They used the ACS F814W and Near-Infrared Camera and Multi-Object Spectrometer (NICMOS) F160W for the size comparison of 27 galaxies with $M_s > 10^{11} M_\odot$ at $0.8 < z < 1.8$, and found that sizes measured in F160W are $19 \pm 7\%$ smaller than those in F814W. Previous optical studies which investigated sizes of disk-like galaxies with $M_s = 10^{10} - 10^{11} M_\odot$ in the rest-frame optical band report that there is no size evolution from $z \sim 1$ to the present (Barden et al. 2005; Trujillo et al. 2007). Our data confirms their result; the circularized sizes of the $z \sim 1$ low- $n(K_s)$ sample measured in the ACS z_{850} -band (rest-frame 4250 Å) are comparable with those of the local galaxies measured in the SDSS g -band (rest-frame 4360 Å) in the same stellar mass range. Combined with the systematic size difference seen in the rest-frame J -band (Figure 8), the $z \sim 1$ disk-like galaxies seem to have a steeper color gradient from the local disk-like galaxies. We show the comparison of the color gradient of disk-like galaxies at $z \sim 1$ and $z = 0$ in Figure 14. For the $z \sim 1$ galaxies with $n(K_s) \leq 2.5$, the sizes in the V_{606} - and z_{850} -band normalized at the K_s -band are plotted. The dotted line is an observed color gradient of local disk-like galaxies (Barden et al. 2005) where the slope, $\alpha = -0.184$, is obtained using the VAGC Sérsic parameters in a similar manner to us. The intercept of the dotted line is determined to make the size at J -band equal to unity. Open squares show the relative sizes of the local disk-like ($n[z] \leq 2.5$) galaxies in our SDSS/VAGC catalog (used in Section 4.2) normalized at z -band and shifted vertically to make the size at z -band lie on the dotted line. We find a steeper slope of the color gradient at $z \sim 1$ than at $z = 0$ by a linear fit with the intercept fixed to unity at the J -band. The slope at $z \sim 1$ derived using the ACS V_{606} , z_{850} , and the MOIRCS K_s -band sizes is $\alpha = -0.77 \pm 0.10$ (-0.97 ± 0.12) and -0.98 ± 0.03 (-0.56 ± 0.03) for the LIRGs and the non-LIRGs in the massive (less massive) sample, respectively. On the contrary, the slope at $z = 0$ derived from u , g , and z -band sizes of our VAGC catalog is $\alpha = -0.19 \pm 0.00$ for the both stellar mass ranges. We note that the linear fit with all the five SDSS bands yields the same slope of -0.19 as with the above three bands. Consequently, the $z \sim 1$ galaxies with $M_s \geq 10^{10} M_\odot$ have 3–5 times steeper color gradient than the local galaxies at the similar stellar mass range. The change in the color gradient between $z \sim 1$ and $z = 0$ can be interpreted as that while the distribution of young stellar population indicated by the rest-frame UV–optical sizes is unchanged from $z \sim 1$ to the present, the structure consisting of old stellar population indicated by the rest-frame

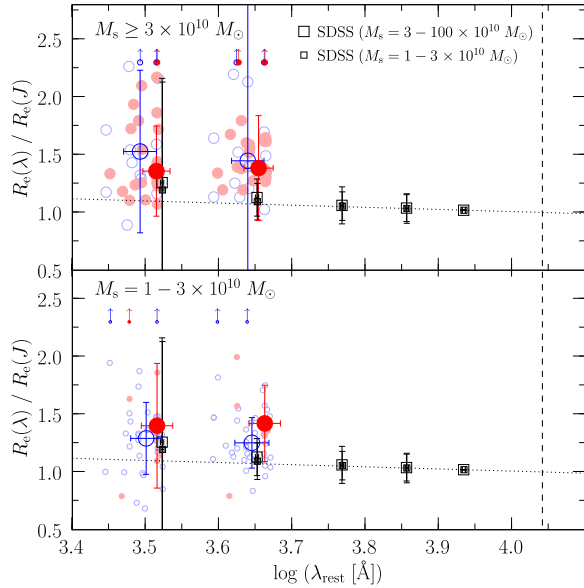


Fig. 14. The normalized effective radii as a function of rest-frame wavelength of the $z \sim 1$ disk-like galaxies. Sizes are normalized at J -band (dashed line). The symbols except for those with error bars and black dots are the same as in Figure 5. The large circles with error bar represent the medians and scatters. Two stellar mass ranges ($M_s \geq 3 \times 10^{10} M_\odot$, $M_s = 1-3 \times 10^{10} M_\odot$) are shown separately. All X-ray-detected galaxies are excluded. Galaxies whose normalized radius is beyond the vertical axis scale are plotted with an up-pointing arrow. The squares with error bar show the median and $1-\sigma$ scatter of the radii for local disk-like galaxies used in Section 4.2. The dotted line represents the color gradient (a slope $\alpha = -0.184$) for local disk-like galaxies (Barden et al. 2005; de Jong 1996) where we set the intercept to make the size at J -band equal to unity.

NIR sizes is still being constructed at $z \sim 1$. Additionally, changes in dust distribution in a galaxy should also contribute to the decrease of the color gradient.

Recent NIR Integral Field Unit (IFU) observations investigating the kinematics of distant ($z \gtrsim 0.6$) disk galaxies revealed that they show a similar Tully-Fisher relation to the local disk galaxies (Flores et al. 2006; Puech et al. 2008; Lemoine-Busserolle & Lamareil 2010). In addition, Neichel et al. (2008) investigated a radial distribution of color and SFR along disk of rotating spiral disk galaxies which show similar morphology and kinematics to the local disk galaxies, and found that the very active and recent star formation is occurred in the outer parts of the disks. They concluded the observational evidence as a rapid, inside-out disk formation of disk galaxies. Our results are consistent with such a disk formation scenario, in which local disk galaxies form their disk structure from the center to the outskirts. Intense star formation activity observed as LIRGs at $z \sim 1$ may be mostly related to the formation and growth of disk structure in relatively massive galaxies, and contribute significantly to the high cosmic SFR density at $z \sim 1$.

6. Summary

In this paper, we studied rest-frame NIR morphologies of galaxies at $z = 0.8-1.2$ from the deep NIR imaging survey (MODS; K09) catalog in a part of the GOODS-N field. The K_s -band image, which is the key data for this work, covers $\sim 28 \text{ arcmin}^2$ and has a PSF $\sim 0''.4$ (FWHM) which corresponds to 3.2 kpc at $z \sim 1$. Cross-correlating our K_s -band galaxy catalog with the *Spitzer*/MIPS 24 μm and the *Chandra* X-ray source catalogs, we identified LIRGs and AGN candidates. Using GALFIT, we performed a two-dimensional light profile fitting of the $z \sim 1$ galaxies in the K_s -band with a single component Sérsic model. Our simulation with artificial galaxy images showed that our morphological analysis is reliable up to $K_s(\text{AB}) \sim 22.5$ mag irrespective of morphology. That magnitude limit corresponds to $M_s \sim 1 \times 10^{10} M_\odot$ at $z \sim 1$ and we adopted that stellar mass as a selection criterion. As a non-parametric morphological study, we measured the Concentration (C) and Asymmetry (A) indices of the galaxies in the K_s -band.

We investigated NIR morphological properties of the 139 galaxies having $z = 0.8-1.2$ and $M_s \geq 1 \times 10^{10} M_\odot$. The main results about those galaxies are summarized as follows.

- $\sim 90\%$ of LIRGs show disk-like ($n[K_s] \sim 1-2$) light profiles in the K_s -band.
- Those low- $n(K_s)$ LIRGs consist of 60% of the whole low- $n(K_s)$ sample above $M_s \geq 3 \times 10^{10} M_\odot$.
- About a half of the low- $n(K_s)$ LIRGs are comparable in size and the others are slightly ($\sim 20\%$ at a maximum) small compared to local disk-like galaxies.
- No correlation between the NIR asymmetry properties and L_{IR} (star formation activity) is found.

Those results indicate that the star formation at $z \sim 1$ is (i) mainly occurred in most relatively massive disk galaxies, and (ii) is not triggered by early-phase strong galaxy-galaxy interactions which disturb strongly the NIR morphology.

In order to investigate how the star formation is occurred in the massive disk-like galaxies, we compared the rest-frame J -band morphologies of the $z \sim 1$ galaxies with the rest-frame U - and B -band ones using the *HST*/ACS V_{606} - and z_{850} -band image, respectively. There is no significant difference in Sérsic index and axial ratio between the rest-frame UV-optical and NIR bands. The comparison of the effective radii shows a $\sim 30\%$ systematic offset where sizes in redder band are smaller. Although this is known as “color gradients” of galaxies in the local universe, the gradient we found is 3–5 times steeper than in the local universe. Since we found the fact that the rest-frame optical sizes of the $z \sim 1$ galaxies are comparable to the local galaxies, this steeper color gradient indicates that fundamental disk structure in those massive galaxies is still being constructed at $z \sim 1$. Our results indicate not only that more than a half of relatively massive disk-like galaxies at $z \sim 1$ are in violent star formation epochs

observed as LIRGs but also that most of those LIRGs are constructing their disk structure vigorously. The high star formation rate density in the universe at $z \sim 1$ may be dominated by star formation in disk region in massive galaxies.

We would like to thank the Subaru Telescope staff for their invaluable help and support for observations. We are grateful to an anonymous referee for many helpful comments and suggestions, that improved our paper. This study is based on data collected at Subaru Telescope, which is operated by the National Astronomical Observatory of Japan. This work is based on in part on observations made with the *Spitzer Space Telescope*, which is operated by the Jet Propulsion Laboratory, California Institute of Technology under a contract with NASA. The Image Reduction and Analysis Facility (IRAF) used in this paper is distributed by the National Optical Astronomy Observatories, which are operated by the Association of Universities for Research in Astronomy, Inc., under cooperative agreement with the National Science Foundation. The SDSS Web Site is <http://www.sdss.org/>. The SDSS is managed by the Astrophysical Research Consortium for the Participating Institutions. The Participating Institutions are the American Museum of Natural History, Astrophysical Institute Potsdam, University of Basel, University of Cambridge, Case Western Reserve University, University of Chicago, Drexel University, Fermilab, the Institute for Advanced Study, the Japan Participation Group, Johns Hopkins University, the Joint Institute for Nuclear Astrophysics, the Kavli Institute for Particle Astrophysics and Cosmology, the Korean Scientist Group, the Chinese Academy of Sciences (LAMOST), Los Alamos National Laboratory, the Max-Planck-Institute for Astronomy (MPIA), the Max-Planck-Institute for Astrophysics (MPA), New Mexico State University, Ohio State University, University of Pittsburgh, University of Portsmouth, Princeton University, the United States Naval Observatory, and the University of Washington.

Appendix 1. Properties of the MODS $z \sim 1$ galaxies

Table 2 is a sample of the information about the properties of the $z \sim 1$ galaxies analyzed in this paper. Columns 1–6 list the basic properties of the galaxy derived from Kajisawa et al. (2009, K09). Column 1 indicates the galaxy identification number. Columns 2 and 3 are the Right Ascension (R.A.) and Declination (Dec.) of the galaxy for epoch J2000 in degrees. Column 4 lists the apparent K_s -band magnitude in the AB system. Column 5 is the measured redshift of the galaxy. Column 6 specifies whether the redshift was determined spectroscopically (s) or photometrically (p). Column 7 is the stellar mass of the galaxy in units of $10^{10} M_\odot$. Column 8 is the MIPS 24 μm flux in units of μJy derived from the 24 μm source catalog (M. Dickinson et al. in preparation; R. Chary et al. in preparation). Possible 24 μm sources which would

be caused by confusion effect identified by visual inspection on the MIPS 24 μm image are denoted by an asterisk. Column 9 is the IR luminosity in units of $10^{11} L_\odot$. Columns 10–14 list the morphological properties of the galaxy measured in the K_s -band. Column 10 indicates the value of the Sérsic index of the fit to the galaxy. Column 11 is the effective radius along the semimajor axis of the galaxy. Column 12 is the axial ratio of the galaxy. And finally, Column 13 and 14 are the concentration and asymmetry indices of the galaxy. Galaxies listed in the X-ray catalog (Alexander et al. 2003) are denoted as “X-ray” in the Comment. The entire catalog for all the 155 galaxies including the X-ray-detected galaxies analyzed in this paper is available as an online material.

Appendix 2. Images of the MODS $z \sim 1$ galaxies

Figure 15 is a sample of postage stamp images and K_s -band surface brightness profiles of the $z \sim 1$ sample analyzed in this paper. In the *left panels*, ACS z_{850} -band (rest-frame B), K_s -band (rest-frame J) images, and K_s -band GALFIT residual image after model subtraction from the K_s -band image are shown from *left to right*. North is to the top and the East is to the left. The size of each image is approximately 5.0×5.0 arcsec ($\sim 40 \times 40$ kpc). The residual image is shown with narrower dynamic range than that for the K_s -band image to display the residual pattern clearly. Simultaneously-fitted neighbors are subtracted from the residual image as well with their best-fit Sérsic models. In the *right panels*, observed (filled circles) and best-fit (solid line) surface brightness profiles in the K_s -band along the semimajor axis are shown in the *top*. The profiles are derived with elliptical isophote fitting package `ellipse` in IRAF. The shape (axial ratio and position angle) and the center of the ellipse are fixed with values derived using GALFIT, and the isophote radius is changed from 0.0 to 2.5 arcsec. The observed profile is derived from the K_s -band image subtracted the simultaneously-fitted neighbors with their best-fit models, and is plotted until the radius reaches 1.5 times the semimajor axial length of the Kron elliptical aperture, which is a criterion for choosing neighbors, or 2.5 arcsec at a maximum. Error bars represent $1-\sigma$ scatter of intensity data along the ellipse at a given radius. The *dot-dashed* line shows the profile of the PSF used in GALFIT normalized to match the brightness with the observed point at the center. A residual of the observed profile is shown in the *bottom*. Image lists for all the 155 galaxies including the X-ray-detected galaxies analyzed in this paper are available as online materials.

References

- Abraham, R. G., Valdes, F., Yee, H. K. C., & van den Bergh, S. 1994, *ApJ*, 432, 75
- Abraham, R. G., Tanvir, N. R., Santiago, B. X., Ellis, R. S., Glazebrook, K., Van Den Bergh, S. 1996, *MNRAS*, 279, 47
- Alexander, D. M., et al. 2003, *AJ*, 126, 539
- Barden, M., et al. 2005, *ApJ*, 635, 959

Table 2. Properties of the MODS $z \sim 1$ galaxies.

ID	R.A. [deg]	Dec. [deg]	K_s (AB) [mag]	Redshift	M_s [$10^{10} M_\odot$]	f_{24} [μJy]	L_{IR} [$10^{11} L_\odot$]	$n(K_s)$	$R_e(K_s)$ [kpc]	$q(K_s)$	$C(K_s)$	$A(K_s)$	Comment	
(1)	(2)	(3)	(4)	(5)	(6)	(7)	(8)	(9)	(10)	(11)	(12)	(13)	(14)	
0072	189.074141	+62.235512	20.51	0.846	(s)	20.9	427.0	4.3	2.2	6.0	0.75	2.94	0.214	
0132	189.159586	+62.197463	20.34	0.841	(s)	10.4	230.0	2.2	0.9	3.3	0.55	2.32	0.040	
0151	189.194153	+62.180282	20.66	0.940	(s)	5.6	354.0	4.7	1.1	1.9	0.60	2.75	0.051	
0152	189.157521	+62.197045	20.32	0.839	(s)	7.0	173.0	1.6	0.7	6.8	0.20	2.41	0.032	
0156	189.153342	+62.203661	18.81	0.848	(s)	47.0	379.0	3.8	2.0	6.6	0.85	2.98	0.029	
0167	189.172377	+62.191551	19.86	0.99	(p)	19.4	287.0	4.3	1.2	4.6	0.80	2.67	0.085	
0227	189.169444	+62.193243	21.35	0.99	(p)	4.2	110.0	1.5	1.0	2.9	0.37	2.45	0.021	
0265	189.131821	+62.212030	21.28	1.016	(s)	2.2	109.0	1.6	1.2	3.5	0.36	2.55	0.032	
0510	189.179991	+62.196678	20.20	1.007	(s)	11.4	113.0	1.6	1.7	3.7	0.66	2.67	0.024	
0658	189.192432	+62.195025	19.36	1.016	(s)	28.6	290.0	4.7	1.3	6.8	0.73	2.56	0.057	

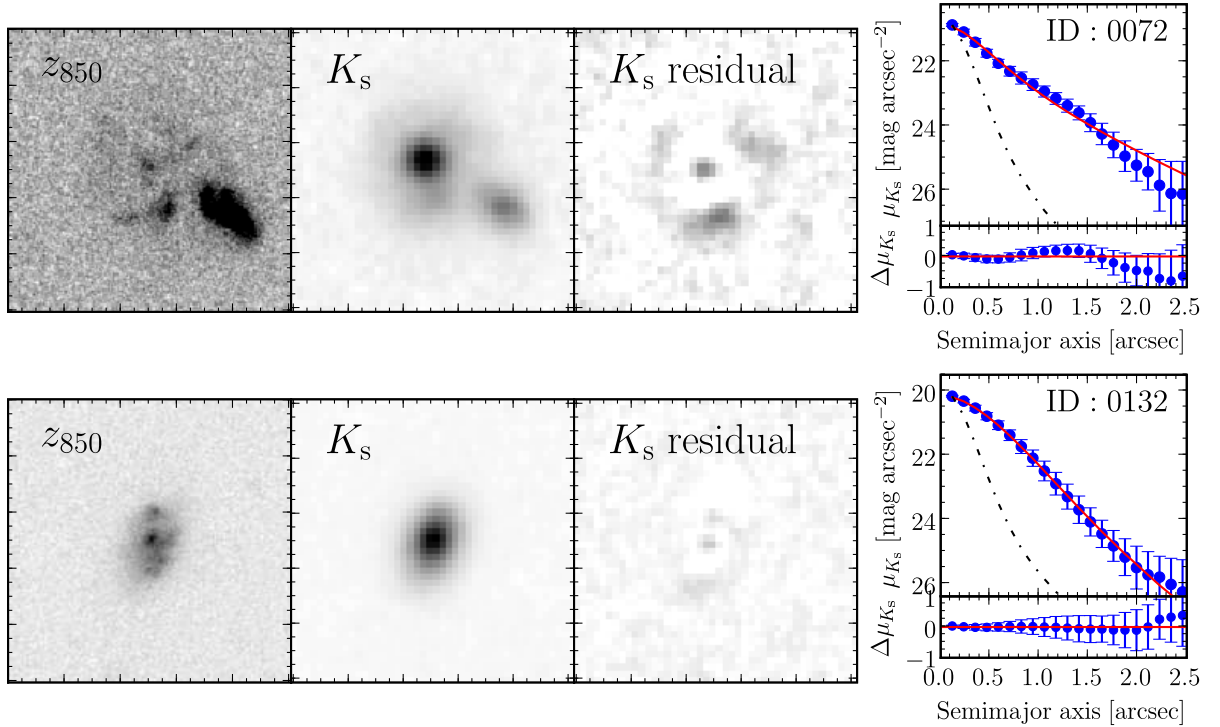


Fig. 15. LIRGs with $n(K_s) \leq 2.5$ at $z \sim 1$ in the MODS deep region. The first two galaxies are shown as a sample. Image lists for all the 155 galaxies including the X-ray-detected galaxies analyzed in this paper are available as online materials. *Left panels:* ACS z_{850} -band (rest-frame B), K_s -band (rest-frame J) images, and K_s -band GALFIT residual image after model subtraction from the K_s -band image are shown from *left to right*. North is to the top and the East is to the left. The size of each image is approximately 5.0×5.0 arcsec ($\sim 40 \times 40$ kpc). The residual image is shown with narrower dynamic range than that for the K_s -band image to display the residual pattern clearly. Simultaneously-fitted neighbors are subtracted from the residual image as well with their best-fit Sérsic models. *Right panels:* Observed (filled circles) and best-fit (solid line) surface brightness profiles in the K_s -band along the semimajor axis are shown in the *top*. The profiles are derived with elliptical isophote fitting package `ellipse` in IRAF. The shape (axial ratio and position angle) and the center of the ellipse are fixed with values derived using GALFIT, and the isophote radius is changed from 0.0 to 2.5 arcsec. The observed profile is derived from the K_s -band image subtracted the simultaneously-fitted neighbors with their best-fit models, and is plotted until the radius reaches 1.5 times the semimajor axial length of the Kron elliptical aperture, which is a criterion for choosing neighbors, or 2.5 arcsec at a maximum. Error bars represent 1- σ scatter of intensity data along the ellipse at a given radius. The *dot-dashed* line shows the profile of the PSF used in GALFIT normalized to match the brightness with the observed point at the center. A residual of the observed profile is shown in the *bottom*.

- Bell, E. F., et al. 2005, *ApJ*, 625, 23
- Bertin, E. & Arnouts, S. 1996, *A&AS*, 117, 393
- Blanton, M. R., et al. 2003, *AJ*, 125, 2348
- Blanton, M. R., et al. 2005, *AJ*, 129, 2562
- Blanton, M. R., & Roweis, S. 2007, *AJ*, 133, 734
- Brinchmann, J., Charlot, S., White, S. D. M., Tremonti, C., Kauffmann, G., Heckman, T., & Brinkmann, J. 2004, *MNRAS*, 351, 1151
- Bruzual, G. & Charlot, S. 2003, *MNRAS*, 344, 1000
- Caputi, K, Lagache, G., Yan, L., et al. 2007, *ApJ*, 660, 97
- Chabrier, G. 2003, *PASP*, 115, 763
- Chary, R., & Elbaz, D. 2001, *ApJ*, 556, 562
- Conselice, C., Bershad, M., Jangren, A. 2000, *ApJ*, 529, 886
- Conselice, C. 2003, *ApJS*, 147, 1
- de Jong, R. S. 1996, *A&AS*, 118, 557
- Flores, H., Hammer, F., Thuan, T. X., et al. 1999, *ApJ*, 517, 148
- Flores, H., Hammer, F., Puech, M., Amram, P., & Balkowski, C. 2006, *A&A*, 455, 107
- Franx, M., van Dokkum, P. G., Schreiber, N. M. F., Wuyts, S., Labbé, I., & Toft, S. 2008, *ApJ*, 688, 770
- Giavalisco, M., et al. 2004, *ApJ*, 600, L93
- Graham, A. W., & Driver, S. P. 2005, *Publ. Astron. Soc. Australia*, 22, 118
- Haarsma, D. B., Partridge, R. B., Windhorst, R. A., & Richards, E. A. 2000, *ApJ*, 544, 641
- Häussler, B., et al. 2007, *ApJS*, 172, 615
- Hogg, D. W., Cohen, J. G., Blandford, R., & Pahre, M. A. 1998, *ApJ*, 504, 622
- Hopkins, P. F., et al. 2004, *AJ*, 128, 1112
- Hopkins, A. M., & Beacom, J. F. 2006, *ApJ*, 651, 142
- Kajisawa, M. et al. 2006, *PASJ*, 58, 951
- Kajisawa, M., et al. 2009, *ApJ*, 702, 1393 (K09)
- Kennicutt, R. C., Jr. 1998, *ApJ*, 498, 541
- Kron, R., G. 1980, *ApJS*, 43, 305
- Le Floch, E., et al. 2005, *ApJ*, 632, 169
- Lemoine-Busserolle, M., & Lamareille, F. 2010, *MNRAS*, in press
- Lilly, S. J., Le Fèvre, O., Crampton, D., Hammer, F., & Tresse, L. 1995, *ApJ*, 455, 50
- Lotz, J. M., Davis, M., Faber, S. M., et al. 2008, *ApJ*, 672, 177
- Madau, P., Ferguson, H. C., Dickinson, M. E., Giavalisco, M., Steidel, C. C., & Fruchter, A. 1996, *MNRAS*, 283, 1388
- Magnelli, B., Elbaz, D., Chary, R. R., Dickinson, M., Le Borgne, D., Frayer, D. T., & Willmer, C. N. A. 2009, *A&A*, 496, 57
- Marcillac, D., Elbaz, D., Chary, R. R., Dickinson, M., Galliano, F., & Morrison, G. 2006, *A&A*, 451, 57
- Melbourne, J., Koo, D. C., & Le Floch, E. 2005, *ApJ*, 632, 65
- Melbourne, J., et al. 2008, *AJ*, 135, 1207
- McIntosh, D., et al. 2005, *ApJ*, 632, 191
- Neichel, B., et al. 2008, *A&A*, 484, 159
- Pannella, M., Hopp, U., Saglia, R. P., Bender, R., Drory, N., Salvato, M., Gabasch, A., & Feulner, G. 2006, *ApJ*, 639, L1
- Peng, C. Y., Ho, L. C., Impey, C. D., & Rix, H. 2002, *AJ*, 124, 266
- Pérez-González, P. G., et al. 2008, *ApJ*, 675, 234
- Pérez-González, P. G., Trujillo, I., Barro, G., Gallego, J., Zamorano, J., & Conselice, C. J. 2008, *ApJ*, 687, 50
- Puech, M., et al. 2008, *A&A*, 484, 173
- Ravindranath, S., et al. 2004, *ApJ*, 604, L9
- Salpeter, E. E. 1955, *ApJ*, 121, 161
- Sanders, D. B. & Mirabel, I. F. 1996, *ARA&A*, 34, 749
- Sanders, D. B., & Ishida, C. M. 2004, *ASPC*, 320, 230
- Sérsic, J.-L. 1968, *Atlas de Galaxias Australes* (Cordoba: Obs. Astron.)
- Seymour, N., Symeonidis, M., Page, M. J., Huhnh, M., Dwelly, T., McHardy, I. M., & Riede, G. 2010, *MNRAS*, in press (arXiv:0911.4134)
- Shen, S., Mo, H. J., White, S. D. M., Blanton, M. R., Kauffmann, G., Voges, W., Brinkmann, J., & Csabai, I. 2003, *MNRAS*, 343, 978
- Suzuki, R., et al. 2008, *PASJ*, 60, 1347
- Symeonidis, M., Page, M. J., Seymour, N., Dwelly, T., Coppin, K., McHardy, I., Rieke, G. H., and Huynh, M. 2009, *MNRAS*, 397, 1728
- Takagi, T., et al. 2010, *A&A*, in press (arXiv:1002.3654)
- Takeuchi, T. T., Buat, V., & Burgarella, D. 2005, *A&A*, 440, L17
- Trujillo, I., Conselice, C. J., Bundy, K., Cooper, M. C., Eisenhardt, P., & Ellis, R. S. 2007, *MNRAS*, 382, 109
- Wang, J. L., Xia, X. Y., Mao, S., Cao, C., Wu, H., & Deng, Z. G. 2006, *ApJ*, 649, 722
- Zheng, X. Z., Hammer, F., Flores, H., Assémat, F., & Pelat, D. 2004, *A&A*, 421, 847
- Zheng, X. Z., Hammer, F., Flores, H., Assémat, F., & Rawat, A. 2005, *A&A*, 435, 507
- Zheng, X. Z., Dole, H., Bell, E. F., Le Floch, E., Rieke, G. H., Rix, H.-W., & Schiminovich, D. 2007, *ApJ*, 670, 301